Catalysis Science & Technology

Stabilization of a Nanoporous NiCu Dilute Alloy Catalyst for Non-oxidative Ethanol Dehydrogenation

Journal:	*Catalysis Science & Technology*
Manuscript ID	CY-ART-04-2020-000683.R1
Article Type:	Paper
Date Submitted by the Author:	02-Jul-2020
Complete List of Authors:	Janvelyan, Nare; Harvard University, Department of Chemistry and Chemical Biology van Spronsen, Matthijs; E O Lawrence Berkeley National Laboratory, Materials Sciences Division Wu, Cheng Hao; E O Lawrence Berkeley National Laboratory, Materials Science Division; University of California Berkeley, Department of Chemistry Qi, Zhen ; Lawrence Livermore National Laboratory, Materials Science Division Montemore, Matthew; Tulane University Department of Chemistry, ; Harvard University Department of Chemistry and Chemical Biology, Shan, Junjun; Tufts University, Zakharov, Dmitri; Brookhaven National Laboratory, Center for Functional Nanomaterials Xu, Fang; Brookhaven National Laboratory, Chemistry Boscoboinik, Jorge; Brookhaven National Laboratory Salmeron, Miquel; Lawrence Berkeley National Laboratory, Materials Science Division; Lawrence Berkeley National Laboratory Stach, Eric; University of Pennsylvania, Materials Science and Engineering Flytzani-Stephanopoulos, Maria ; Tufts University, Department of Chemical and Biological Engineering Biener, Jürgen; Lawrence Livermore National Laboratory Friend, Cynthia; Harvard University, Chemistry and Chemical Biology; Harvard University, Rowland Institute

ARTICLE

Stabilization of a Nanoporous NiCu Dilute Alloy Catalyst for Non-oxidative Ethanol Dehydrogenation

Received 00th January 20xx,
Accepted 00th January 20xx

DOI: 10.1039/x0xx00000x

Nare Janvelyan[a], Matthijs A. van Spronsen[a,b], Cheng Hao Wu[b], Zhen Qi[c], Matthew M. Montemore[d,†], Junjun Shan[e,‡], Dmitri N. Zakharov[f], Fang Xu[a], J. Anibal Boscoboinik[f], Miquel B. Salmeron[b,g], Eric A. Stach[f,§], Maria Flyztani-Stephanopoulos[e], Juergen Biener[c,*], and Cynthia M. Friend[a,d]

Producing acetaldehyde, an important industrial chemical, by direct catalytic non-oxidative dehydrogenation of ethanol presents many advantages over current production methods, including generating hydrogen. However, a stable, active, and selective catalyst is currently unavailable. This work demonstrates that the high activity and selectivity of nanoporous (np) NiCu for this reaction can be stabilized by keeping the catalyst in a metastable ("kinetically trapped") state. Using a combination of in situ ambient-pressure and ex situ X-ray photoelectron spectroscopy, environmental transmission electron microscopy, and density functional theory calculations enabled correlating changes in surface composition with the changes in activity and stability upon treatment of np NiCu with H_2 and O_2. Reduction of Ni-doped nanoporous Cu by H_2 exposure enhanced the initial activity but led to complete catalyst deactivation within ~40 hours. Contrasting, O_2 pretreatment of the same catalyst increased both activity and long-term stability, with only 15% activity loss over 40 hours. The stability of np NiCu as a catalyst inversely correlates with the amount of metallic Ni at the surface, which is enriched by the H_2 pretreatment, while the O_2 pretreatment leads to a kinetically trapped Ni^{2+} subsurface state. This work emphasizes that detailed understanding of pretreatment-induced nanoscale structural and compositional changes is necessary to optimize catalyst performance.

1. Introduction

Improvements in the energy efficiency of chemical production is urgently needed to meet global energy challenges. Heterogeneous catalysis using nanomaterials has the potential for substantially increasing efficiency through enhancement of reaction selectivity and decreasing the operating temperature for high-volume processes. Nanomaterials may also enable new catalytic processes that improve efficiency by eliminating the need for separation of byproducts, such as water.

The production of acetaldehyde is a good example demonstrating the need to improve the energy efficiency of chemical transformations. Acetaldehyde is a starting material for several industrial chemicals, including acetic acid, acetate esters, pentaerythritol, pyridine, and pyridine-based compounds.[1, 2] In 2015, (1–2)×10^5 tons of acetaldehyde were produced in the USA.[3] A major pathway for industrial production of acetaldehyde is the oxidative dehydrogenation of ethanol catalyzed by silver,[1, 2] which requires high temperature (500–650 °C) and separation of the byproduct, water. A potential alternative is non-oxidative ethanol dehydrogenation catalyzed by Cu-based materials, which generates H_2, a clean fuel, as a byproduct instead of water.[4-17] Unfortunately, the use of Cu for non-oxidative acetaldehyde production is not yet practical because of low conversion[6] and catalyst deactivation by sintering[8, 12, 14] or carbon deposition.[9]

Nanoscale copper alloys catalysts have been studied for improving stability, yet they have not been adopted: CuCr alloys are not used for environmental reasons,[5] Cu alloyed with alkali metals showed negligible improvement in stability,[6] and CuAg was not selective for acetaldehyde[18] or did not (significantly) improve the activity.[8, 15] However, NiCu (<3 at.% Ni) nanomaterials have recently been shown to be active and selective for non-oxidative ethanol dehydrogenation to acetaldehyde and hydrogen. The Ni dopant lowers the apparent activation energy, and nearly 100% selectivity is retained as long as Ni is atomically dispersed.[19-21] Catalysts composed of Ni and Cu are of wide importance because of their use in many catalytic and electrocatalytic applications (including CO_2 reduction). They are also earth-abundant and relatively inexpensive.

The function and stability of nanoscale alloy catalysts, such as NiCu, rely on the structure and composition of their surface. Hence, understanding and controlling the evolution of the catalyst surface

[a] Department of Chemistry and Chemical Biology, Harvard University, Cambridge, MA 02138, USA.
[b] Materials Sciences Division, Lawrence Berkeley National Laboratory, Berkeley, CA 94720, USA.
[c] Nanoscale Synthesis and Characterization Laboratory, Lawrence Livermore National Laboratory, Livermore, CA 94550, USA.
[d] John A. Paulson School of Engineering and Applied Sciences, Harvard University, Cambridge MA 02138, USA
[e] Department of Chemical and Biological Engineering, Tufts University, Medford, MA 02155, USA
[f] Center for Functional Materials, Brookhaven National Laboratory, Upton, NY 11973, USA
[g] Department of Materials Science & Engineering, University of California, Berkeley, CA 94720, USA
*Corresponding author (biener2@llnl.gov)
†Current address: Department of Chemical and Biomolecular Engineering, University, Tulane University, New Orleans, LA 70118, USA
‡Current address: NICE America Research Inc. Mountain View, CA 95120, USA
§ Current address: Department of Materials Science and Engineering, University of Pennsylvania, Philadelphia, PA 19104, USA

Electronic Supplementary Information (ESI) available: Additional reactivity data, X-ray photoelectron spectra, and electron microscopy images. See DOI: 10.1039/x0xx00000x

structure and composition during activation, catalytic cycle, and deactivation has been defined as a research priority in catalysis.[22] For example, gas-phase induced surface segregation has been used to tune the surface composition and catalytic activity of various nanomaterials.[23-27] While the importance of pretreatments on the formation of active sites is well established, the physical, mechanistic, and kinetic details of these dynamic materials largely remain as open questions.

Using *in situ* and *ex situ* X-ray photoelectron spectroscopy and various electron-microscopy techniques, this work demonstrates that the catalytic activity and stability of a nanoporous (np) NiCu alloy catalyst can be improved by generating a kinetically trapped Ni^{2+} subsurface state through an O_2 pretreatment. Exposure of the oxidized surface to ethanol at reaction temperature reduces the CuO surface while most of the Ni remains oxidized and embedded in the Cu. In this state, Ni doping provides stable (over 60 hours) and improved activity for catalytic dehydrogenation of ethanol to acetaldehyde and hydrogen. While the O_2 pretreatment buries Ni oxide under a Cu oxide overlayer, a H_2 treatment causes the formation of Ni-rich nanoparticles on the surface. This H_2-treated np NiCu catalyst completely deactivates within ~40 hours on stream, possibly related to the deposition of carbon on the catalyst surface.

2. Methods

2.1 Catalyst Preparation

Unsupported nanoporous Cu (np Cu) and Ni-doped np Cu (np NiCu) samples were prepared by dealloying and wet-impregnation techniques. Using unsupported np Cu and np NiCu allows us to evaluate the activity and stability of these catalysts without interference from support materials. Np Cu with a porosity of ~80% (not accounting for potential sample shrinkage) was prepared by selective etching of Zn from $Zn_{80}Cu_{20}$ alloy ingots (12 mm × 3 mm × 1 mm) in 5 M hydrochloric acid (50 mL). The samples were dealloyed at room temperature for 4 days and then dealloyed for one more day with fresh etch solution. The nanoporous structure of the material spontaneously develops during selective etching of the Zn. After dealloying, the samples were rinsed with deionized water at least three times and dried in a desiccator under vacuum at room temperature for 3 days. The resulting np Cu contains about 5 at.% residual Zn, as determined by inductively coupled plasma mass spectrometry (ICP-MS) and energy-dispersive X-ray spectroscopy (EDS).

Ni doping was achieved by submerging np Cu samples in 2 mL of a 0.3 M nickel (II) nitrate solution. The glass vial with the sample was then placed in a desiccator for 2 h at room temperature to ensure full penetration of the pores with the Ni nitrate solution. To preserve the uniformity of the Ni distribution through the drying process, the Ni-solution-infilled np Cu sample was then immersed in liquid nitrogen for 1 minute and then placed in a freeze-drying system at 0.01 Torr and –106 °C (Labconco, FreeZone 4.51 Benchtop Freeze Dry System) for 2 days. Finally, to reduce the Ni salt residue and to warrant uniform Ni-Cu alloy formation, the Ni impregnated np Cu samples were annealed for 1h at 500 °C in 4% H_2 in Ar at 760 Torr. The annealing time (1h) and temperature (500 °C) were chosen based on the reported interdiffusion constants[28] for the Ni-Cu system so that the diffusion length (700 nm) is larger than the ligament size (~300 nm) while minimizing ligament coarsening. This reduction/alloying step is considered part of the synthesis procedure and is not considered a "pretreatment" as discussed in the main text.

Based on the concentration of the Ni salt solution (0.3 M) and the porosity of the np Cu samples (80 %), this procedure is expected to result in a Ni-doping level of ~1 at.% (if only the Ni from the Ni nitrate solution within the pores is deposited on the np Cu sample).

The average volumetric Ni concentration of 1 at.% was verified in previous work by ICP-MS.[19, 21] In this work, X-ray photoelectronspectroscopy (XPS) performed on crushed samples reveals an average Ni concentration of ~3 at.% Ni near the ligament surface (Table S1) while a Ni concentration of ~6 at.% was found at the outer surface of the bulk np-NiCu samples, which can be attributed to some excess Ni solution at the sample surface. The np Cu and np NiCu bulk samples were used as prepared for AP-XPS studies. For all other techniques, samples were crushed into a powder.

2.2 Catalytic Activity

Catalytic performance was measured in a quartz tube reactor housed in a temperature-controlled furnace operated at atmospheric pressure. Ultrahigh-purity (99.99%) gases were supplied to the reactor by mass-flow controllers. Hydrogen treatment was performed by flowing a mixture of 10% H_2 in He at 20 mL $minute^{-1}$ at room temperature, followed by ramping the temperature to 350 °C at 10 °C $minute^{-1}$ and holding it at 350 °C for 1 h. Oxygen treatments were performed at 250 °C using 20% O_2 in He at a flow rate of 50 mL $minute^{-1}$ for 1 h. The ethanol dehydrogenation reaction was performed using 6% ethanol (Sigma Aldrich, ≥ 99.5%) in He with a 50 mL $minute^{-1}$ total flow rate at 250 °C by flowing a He stream through a bubbler filled with ethanol at room temperature. The effluent gas was monitored by an online gas chromatography-mass spectrometry (GC-MS) instrument (Agilent 5975C and Agilent 7890A) equipped with HP-PLOT Q and CARBONPLOT columns. The effluent gas was also monitored by an online residual-gas analyzer (Hiden HAL 3F RGA). Np (Ni)Cu samples (~30 mg) were crushed prior to catalytic testing, although no difference was observed when intact np (Ni)Cu samples were used, demonstrating the absence of mass transport limitations.

2.3 *Ex situ* XPS, SEM, and STEM

Ex situ XPS was performed using a Thermo Scientific K-Alpha XPS setup with a monochromatic Al Kα source. XPS samples of crushed np (Ni)Cu samples were prepared by loading the catalyst particles onto carbon tape and analyzed after each specified treatment. Scanning electron microscopy (SEM) was performed using a Zeiss Supra55VP field-emission SEM equipped with an EDS detector. Scanning transmission electron microscopy (STEM) and EDS mapping were performed using an aberration-corrected JEOL ARM 200F STEM as well as a FEI Talos F200X. To prepare STEM samples, powder samples were dispersed in deionized water and drop cast onto lacey C/Au mesh grids (Ted Pella, Inc).

2.4 Environmental Transmission Electron Microscopy

Environmental transmission electron microscopy (E-TEM) studies were conducted using a FEI Titan aberration-corrected transmission electron microscope operating at 300 kV with electron energy-loss spectrometry (EELS) capabilities. Because of the overlap of the Cu and Zn $L_{2,3}$ edges, EELS could not be used to detect Zn, the minority species. The instrument had a base pressure of (3.5 ±0.5) × 10^{-7} Torr. Samples in powder form were dispersed in deionized water and drop cast onto a sample holder (DENS Solutions). After drying, the holder was inserted in the microscope. Gases and vapors were introduced into the microscope using a gas-handling manifold equipped with

dosing valves with the beam blocked. The sample was then heated to the specified temperatures and held for the treatment duration. After cooling, the gases were evacuated to reach vacuum for imaging and EELS analysis.

2.5 Ambient-Pressure X-ray photoelectron spectroscopy

AP-XPS experiments were conducted at beamline 23-ID-2 at the National Synchrotron Light Source II at Brookhaven National Laboratory. Because the freeze-drying synthesis step resulted in slightly inhomogeneous Ni concentrations across the np NiCu samples, both surface and cross-section of the samples were studied (Figure S3a), resulting in qualitatively similar behavior; thus, only the outer surface is discussed in the main text for simplicity. Quantification of the composition of the surface and cross-section are provided in the supplementary information (SI, Table S1). Quantification of Ni oxidation states are also provided in the SI (SI, Table S2).

As-prepared np (Ni)Cu samples were used to investigate *in situ* H_2 treatment (350 °C, 1 Torr, 1 h) by AP-XPS. For the catalytic AP-XPS studies, a np NiCu sample H_2-pretreated in the flow reactor (350 °C, 10% H_2/He at 760 Torr, 1 h) was used to study the effect of the following sequence of treatments: exposure to ethanol (250 °C, 0.2 Torr, 6 h), O_2 (250 °C, 1 Torr, 1 h), and ethanol again (250 °C, 0.2 Torr, 1 h). Samples were analyzed in ultra-high vacuum at room temperature after specified exposures unless otherwise noted. The beam was blocked during gas exposure and between spectra collection to minimize beam-induced artefacts.

To ensure that the same depth was probed for each element, the X-ray energy was varied such that the kinetic energy of all photoelectrons was around 200 eV. Every time the photon energy was changed, the spectrum was calibrated to the Fermi edge. Spectral analysis details are provided in the SI (Figure S3b). The inelastic mean free paths for the photoelectrons for the np NiCu material were approximated by using the values for pure Cu, the majority component.[29]

Near-edge X-ray absorption fine structure spectra were acquired using the hemispherical analyzer in partial electron yield mode. For the Cu and Ni L-edge spectra, the kinetic energies of the measured photoelectrons were selected to be 320 eV and 240 eV, respectively, similar to that of the AP-XPS and such that no XPS or Auger peaks appear within the scanned energy range, which would otherwise produce false NEXAFS peaks.

2.6 Density Functional Theory

Density-functional theory (DFT) calculations were performed with the VASP code,[30, 31] the PBE exchange-correlation functional,[32] and the projector-augmented wave method.[33, 34] The Tkatchenko-Scheffler method was used for dispersion corrections.[35] A 400-eV planewave cutoff was used in all cases. A Cu(110) surface was used to model the reduced catalyst surface and the CuO(111) surface was used to model the oxidized surface. For the Cu(110) surface, a (3×2) surface cell was used to model the surface, and the Brillouin zone was sampled with a 7×7×1 k-point mesh. For the CuO(111) surface, a (2×2) surface cell was used, with a 4×4×1 k-point mesh. U values were taken from previous work (4 eV for Cu and 6 eV for Ni),[36] as was the antiferromagnetic structure.[37] Spin polarization was employed in all calculations.

To explore the effect of adsorbed oxygen and hydrogen on the Ni distribution, Ni atoms were placed in the first to third layers of the Cu(110) surface with hydrogen and oxygen coverages ranging from 0 to 1 monolayer (ML), and the furthest extreme of a full copper oxide, CuO(111) surface. We also modeled a Ni monolayer, in place of Ni atoms, placed in the first to third layers of Cu(110) surface with varying oxygen coverage and the CuO(111) surface. Relative surface energies were calculated by subtracting the total energy of the structure with Ni in the fourth layer from the total energy of each structure (Table S4). Because the number of each atom type is preserved, this corresponds to a difference in the surface energies. Surface energies of Ni in the third layer were roughly the same as the fourth layer and thus are not included.

3. Results

3.1 Catalytic Activity

The as-prepared nanoporous dilute Ni-Cu alloy (np NiCu) has an interconnected ligament-and-pore structure with a ligament diameter of 305±85 nm (SI, Figure S1). As previously demonstrated, residual Zn from the CuZn starting alloy does not affect the activity of np Cu and np NiCu.[19, 38] Although some activity of Zn in oxidized form or its interface with Cu cannot be excluded.[10, 16]

Catalytic tests of np Cu and np NiCu catalysts for non-oxidative ethanol dehydrogenation towards acetaldehyde and H_2 reveal that (1) Ni doping increases the activity and (2) the stability of Ni as a promotor strongly depends on the catalyst pretreatment (**Figure 1**). Conversely, the catalytic activity of np Cu is essentially the same for both H_2 (350 °C) and O_2 (250 °C) pretreatments with stable, non-oxidative ethanol-to-acetaldehyde conversion with 100% selectivity for 60 h (Figure 1a and S2a), except for the first 10 h. In this transient regime, the O_2 pretreated np Cu (O_2-np Cu) shows a markedly increased activity (red, Figure 1a), which can be attributed to the reaction of ethanol with Cu oxides, as reported in the literature[4, 39, 40] and observed by XPS and E-TEM in the sections to follow.

Pretreatment of np NiCu with O_2 (O_2-np NiCu) yields a catalyst that is more active than either H_2-pretreated np NiCu (H_2-np NiCu) or np Cu itself (Figure 1). Whereas H_2-np NiCu rapidly and completely deactivates in reaction conditions, the O_2 pretreatment stabilizes the catalyst for acetaldehyde production (red, Figure 1b). Like O_2-np Cu, O_2-np NiCu shows enhanced activity in the initial transient regime (<10 h). The transient regime is followed by relatively stable operation with only a modest activity loss of 15% between 10 and 40 h, after which point the activity is still 40% higher than that of the corresponding undoped np Cu catalyst (red, Figure 1a). Even after 60 h on stream, O_2-np NiCu is still 38% more active than np Cu (Figure S2b). By contrast, H_2-np NiCu completely deactivates after 40 h on stream. Coarsening does not seem to contribute to the deactivation of H_2-np NiCu or the modest 15% activity loss of O_2-np NiCu as the ligament/nanopore feature size remains very similar for both H_2 (Figure S1a,b) and O_2 (Figure S1c,e) pretreated samples before and after being 45/40 h on stream. It is also important to note that while previous work[19] showed that H_2-np NiCu remains stable under lower conversion rate conditions using lower reactant flow rates, 7.5 ml/min instead of 50 ml/min in this work, the O_2 pretreatment is critical in stabilizing the high activity of np NiCu at higher conversion rates. Both H_2- and O_2-treated np NiCu catalysts maintain 99% selectivity to acetaldehyde during the time on stream with by-products being CO and CH_4.

Hydrogen treatment promptly deactivates the active, O_2-np NiCu catalyst (red, Figure 1b). With subsequent time on stream, the

catalyst loses 95% of its initial activity, like H_2-np NiCu, demonstrating the detrimental effect of the H_2 treatment on the Ni-doped catalyst. Interestingly, the H_2 treatment initially and transiently increases the activity, which may be attributed to cleaning of the surface by hydrogen.[41]

3.2 X-ray Photoelectron Spectroscopy and Scanning Electron Microscopy

While neither the H_2 nor the O_2 pretreatment changes the morphology of the np NiCu pore-ligament network, they strongly affect the ligament surface composition and oxidation state of Ni and Cu. To follow these changes, *in situ* studies were conducted using ambient-pressure X-ray photoelectron spectroscopy (AP-XPS) and near-edge X-ray absorption fine structure (NEXAFS) analysis (for details see Section S1 and Figure S3 regarding sample loading and section S2 for spectral analysis). As noted above, the residual Zn (Figure S4) from the CuZn starting alloy has previously been shown to not affect the activity of np Cu and np NiCu.[19, 38]

After *in situ* H_2 treatment (350 °C, 1 Torr, 1 h), both Cu and Ni are completely reduced based on XPS (Figure 2a, i–iii) and NEXAFS analysis (Figure S5a), and SEM reveals a smooth ligament surface (Figure 2a, v). AP-XPS performed with a higher inelastic mean free path (IMFP) of 1.2–1.3 nm proves that the *in situ* H_2 treatment also fully reduced Cu and Ni in subsurface layers (Figure S6). The H_2 treatment drives Ni to the surface increasing the Ni/Cu surface ratio from 0.07 (5.6 at.%) Ni (considering Ni, Cu, and Zn) for the as prepared sample to 0.16 (11.3 at.%) Ni after H_2 treatment (Figure 2a, iii and Table S1). This behavior is consistent with previous studies that demonstrate that Ni migrates to the surface driven by the formation of strong Ni–H bonds.[42-45] Note that Ni surface enrichment does not require operation of Ni bulk diffusion but can be explained by lower activation barrier surface diffusion and place exchange processes. The AP-XPS data also prove that both metals fully reduce in the flow reactor where the H_2 partial pressure is much higher (76 Torr *vs*. 1 Torr). The large metallic component in the *ex situ* Ni 2p XPS confirms that Ni remains mostly reduced even after intermittent exposure to air (Figure 2a, iv).

Exposure of np NiCu to O_2 (250 °C, 1 Torr, 1 h) leads to the formation of a Cu^{2+} oxide (CuO) surface layer that buries the Ni (Figure 2b, i–iii). With an IMFP of 0.6 nm, Ni is below the detection limit of XPS (<2 at.%) (Figure 2b, iii). A small amount of Ni^{2+} is detected by *ex situ* XPS (Figure 2b, iv), because of the higher IMFP of 1.2 nm, indicating Ni is still present below the thin CuO surface layer and that the O_2 treatment oxidized Ni during the overgrowth with CuO. The formation of the Cu oxide roughens the surface of the ligaments while maintaining the overall ligament structure (Figure 2b, v).

Ethanol exposure (0.2 Torr at 250 °C for 1 h) of O_2-np NiCu reduces most of the copper oxide overlayer (Figure 2c, i), and Ni becomes detectable again (Figure 2c, ii). NEXAFS analysis revealed that 29% of the copper in the copper oxide overlayer becomes reduced to the Cu^{1+} state with the rest being Cu^0 (Figure S5c). Based on the reported reduction kinetics of copper oxides,[46] Cu is expected to completely reduce to Cu^0 under reaction conditions, and the presence of Ni should further facilitate the reduction of Cu oxide.[47, 48] The reduction of the Cu oxide coincides with the transient enhancement in catalytic activity during the first few hours on stream (6 vol.% ethanol in He at 1 atm; Figure 1b) indicating the reaction of ethanol with Cu oxide surface species[40]. As the Cu oxide surface layer is reduced by ethanol exposure, the rough surface morphology formed during the O_2 pretreatment smoothens (Figure 2c, v), and continues to become smoother with increasing time on stream (Figure S7).

As most of the Cu surface oxide is reduced by ethanol exposure, oxidized Ni surface species become detectable again. After 1 h of ethanol exposure (0.2 Torr) of O_2-np NiCu (Figure 2c, iii), the Ni surface concentration is ~5 at.% Ni (0.06 Ni/Cu ratio), less than half of what was detected on H_2-np NiCu after 6 h of ethanol exposure (0.2 Torr) (Table S1). Least square fitting of the Ni 2p spectrum of O_2-np NiCu after 1 h of ethanol exposure (0.2 Torr) indicates a mixture of metallic Ni (19%), NiO (36%), and $Ni(OH)_2$ (45%); thus nearly 80% of the near-surface Ni remains in the oxidized Ni^{2+} form (Table S2). Even after 6.5 h of ethanol exposure (0.2 Torr), over half the Ni still is in the 2+ oxidation state (Figure S8 and Table S2). After 40 h of ethanol exposure (6 vol.% ethanol in He at 1 atm), during which the catalyst remained active unlike its H_2-treated counterpart, the *ex situ* Ni 2p spectrum reveals a large Ni^{2+} component that cannot be attributed to air exposure (Figure 2c, iv). Kinetic studies of Ni oxide reduction indeed confirm that Ni^{2+} does not fully reduce on this timescale at the low reaction temperature of 250 °C with ethanol or even with H_2, thus keeping Ni^{2+} in a kinetically trapped state.[49, 50]

Without the O_2 pretreatment, ethanol-exposed (250 °C, 0.2 Torr, 6 h) np NiCu exhibits metallic Cu and Ni 2p XPS (not shown) and NEXAFS L-edge spectra (Figure S5b) like H_2-np NiCu. Consistent with previous work,[19] the Ni/Cu surface ratio of np NiCu stays constant during ethanol exposure (0.2 Torr), in this case at about 0.16 (Table S1). Even though the ethanol pressure under AP-XPS conditions is two orders of magnitude lower than in the catalytic studies (Figure 1), detection of H_2 and acetaldehyde by mass spectroscopy confirms that the catalyst is active, and ethanol is being dehydrogenated (Figure S9a).

XPS spectra also indicate the accumulation of carbon during ethanol reduction on np NiCu, hinting at a possible mechanism for the rapid deactivation of the H_2 pretreated np NiCu sample (Figure 1b). C 1s spectra taken in ultra-high vacuum and room temperature before and after the AP-XPS ethanol exposure demonstrate a pronounced increase in carbon-to-metal signal after ethanol exposure (Figure S9b). The amount of carbon accumulating on the H_2-np NiCu correlates with the Ni concentration, with more carbon (and Ni) on the surface of the monolithic np NiCu sample than on the cross section (Table S3). The accumulation of carbon must have occurred during reaction as carbon deposition by X-ray-beam-assisted fragmentation of ethanol can be ruled out as the spectra were recorded after evacuating the ethanol.

3.3 Transmission Electron Microscopy

The primary structural feature observed by E-TEM after *in situ* reduction in H_2 (350 °C, 1 Torr, 1 h) and ethanol exposure (250 °C, 0.2 Torr, 17 h), similar to the AP-XPS conditions, is the presence of nanoparticles at the ligament surface of the np NiCu catalyst (Figure 3a). Electron energy-loss spectroscopy (EELS) scans (Figure 3c) reveal that the particles consist mostly of Ni embedded in metallic Cu (Figure 3c, i–iii).[51]

After *in situ* oxidation (250 °C, 1 Torr, 1 h), nanoparticles are no longer observed at the surface (Figure 3b). Instead, a rough surface layer formed filling the previously observed trough, though the general shape of the ligament is preserved. EELS analysis reveals that the rough surface layer consists of copper oxide, identified by the peak at 933 eV (Figure 3c, iv). Metallic copper is still present in the

bulk of the ligament, suggested by the shape of the curve (Figure 3c, v), and Ni was no longer detected.

Ex situ scanning transmission electron microscopy (STEM) and energy-dispersive X-ray spectroscopy (EDS) mapping of active, O_2-np NiCu after 40 h of ethanol exposure shows that Ni-rich nanoparticles reemerged at the surface (Figure 3d). The surface particles appear gray in the STEM image, indicating a lower Z-contrast oxidized nature of these particles, consistent with the AP-XPS results. The EDS map shows that while Ni is concentrated within the particles (blue) it also is dispersed in the Cu bulk (orange). Closer inspection of the individual Cu and Ni elemental maps (Figure S10), reveals overlapping areas of Cu and Ni at the ligament edge confirming that Ni is also present in the form of a dilute NiCu alloy in addition to oxidized Ni-rich particles at the surface. Because of the decreased Ni content at the surface after oxidation (Table S1), the Ni-rich particles likely partially reemerge at surface as the Cu oxide reduces and reverts to a smooth surface.

Characterization of deactivated H_2-np NiCu reveals that the nanoparticles remain present at the surface throughout ethanol exposure. These particles are dense and white in the STEM image indicating their metallic nature (Figure 3e). The EDS map shows a large concentration of Ni (blue) within the particles as well as dispersed Ni in the Cu (orange). Quantification of the EDS spectra reveal that the particles contain 20±10 at.% Ni, while the ligament contains 1 at.% Ni (Figure S11). The Ni content of the particles is in large excess to the bulk Ni-doping (~1 at.%) and the surface Ni content detected by AP-XPS after H_2 and ethanol exposures (11 at.%) (Figure 2a, Table S1). Therefore, the surface Ni enrichment driven by H_2 treatment is largely concentrated in the form of metallic, Ni-rich alloy particles at the surface. It is likely that the presence of these metallic, Ni-rich alloy particles is responsible for the accumulation of carbon observed during ethanol reduction on the H_2-pretreated np NiCu sample (Figure S9b) and the concurrent rapid deactivation (Figure 1b).

3.4 Density Functional Theory

The results from DFT calculations are consistent with the notion that surface hydrogen provides a driving force for migration of Ni to the surface and that the driving force for this Ni surface migrations increases with increasing hydrogen coverage (**Figure 4**a). Without adsorbates, Ni is more stable in the Cu bulk than at the Cu surface, in agreement with previous studies.[42, 45, 52] As the H coverage increases to 0.17–0.33 ML, Ni prefers the second layer compared to the fourth layer by ~0.2 eV (Table S4). At a H(ads) coverage of 1 ML, Ni in the surface layer is more stable than Ni in the second layer by 0.4 eV. Therefore, as the surface H coverage increases, the driving force for Ni surface enrichment increases.

Increasing the O surface coverage also provides a driving force for the migration of Ni from the bulk to the surface (Figure 4b). For low oxygen coverages up to 0.2–0.3 ML, Ni is more stable in the second layer compared to the first layer by 0.13 eV (Figure 4b and Table S4). With further increasing O coverage (0.33–1 ML), Ni starts to prefer the first layer.

However, if the Cu surface is completely oxidized to CuO, the most stable structure has Ni in the second layer under the CuO surface layer. Modeling of a Ni monolayer to more closely resemble the high Ni concentration observed in the nanoparticles reveals a similar trend to that observed for isolated Ni atoms: Ni prefers the fourth layer without adsorbates, the topmost layer with 1 ML of O(ads), and the second layer in the case of a CuO surface layer (Table S4).

We studied only a limited number of configurations and, thus, it cannot be ascertained that we identified the minimum energy configurations. Nevertheless, our DFT results provide qualitative evidence that and how Ni surface segregation in NiCu alloys can be driven by changes in the adsorbate coverage and the oxidation states of the alloy, thus providing insight into conflicting reports of surface segregation in these alloys. At O_2 pressures lower than 10^{-4} Torr, O adsorption and Ni segregation is observed at the surface of NiCu alloys with various compositions, consistent with our DFT model (Figure 4b).[52-54] Exposure of NiCu alloys to O_2 pressures above 10^{-4} Torr results in CuO segregation at the surface,[44, 45, 55-58] consistent with our experimental observations and our DFT model that shows that Cu becomes more stable after oxidation. One study demonstrated that with increasing O_2 exposure, from 10 to 10^4 Langmuir (defined as 1×10^{-6} Torr s), the NiO segregation at the surface progressively decreased until the surface had less Ni than the bulk concentration, essentially observing copper segregation at the surface.[54] Although different conditions were used in these studies, surface segregation was most sensitive to pressure. The oxygen coverage and DFT studies reflect an underlying principle that is often overlooked and extends to other alloy systems: It is the amount of oxygen adsorbed that governs which component segregates to the surface. Further, trends in surface segregation are not necessarily monotonic in gas exposure, as the oxide will behave differently from a metal surface with adsorbed oxygen.

A copper oxide overlayer covering the surface may seem surprising as the high affinity of Ni for oxygen provides a driving force for Ni surface migration.[52-54] However, adsorbed oxygen also mobilizes Cu surface atoms.[59, 60] The disappearance of Ni during the O_2 pretreatment can also be explained by growing a Cu oxide surface layer covering the Ni surface atoms rather than by inward migration of Ni away from the surface.[44, 55-58] For example, complete overgrowth of an initially formed nickel oxide by copper oxide was observed for a $Cu_{60}Ni_{40}$ alloy after 30 minutes of O_2 exposure (0.4 Torr) at 250 °C.[57] Therefore, it is reasonable that copper oxide overgrew Ni with 1 Torr O_2 at 250 °C after 1 h in the np NiCu catalyst, in agreement with DFT model (Figure 4) as they reveal that the migration of Ni to the bulk from a Cu oxide surface is relatively favorable.

4. Discussion

Our experiments demonstrate that even low Ni concentrations increase the catalytic activity of Cu consistent with previous studies.[9, 11, 61-63] For ethanol dehydrogenation to acetaldehyde and H_2, isolated Ni atoms in Cu are the active site for the rate-determining C_α-H bond cleavage,[7] lowering the activation energy and increasing the activity of Cu for this reaction.[20] NiCu alloys with 0.1 to 1 at.% Ni contain isolated Ni atoms and maintain near-100% selectivity to acetaldehyde.[19, 20] The question remains why the H_2 treated sample deactivates so quickly while the O_2-treated sample not only shows enhanced activity but also long-term stability. The above presented results show that H_2 pretreatment of the np NiCu catalyst leads to Ni surface segregation and Ni cluster formation, while the O_2 pretreatment leads to the growth of a Cu oxide surface layer that buries oxidized Ni. Subsequent exposure to ethanol under reaction conditions reduces the Cu oxide surface layer, in accordance with *in situ* infrared measurements[12] and analysis of

spent catalysts.[12, 17] Simultaneously, most of the Ni stays in a kinetically trapped Ni^{2+} state. The difference in the reduction behavior of Cu and Ni species under reaction conditions reflect the higher Ni-O bond dissociation energy (366 kJ/mol) compared to Cu-O (287 kJ/mol).[64] Our results suggest that the improved long-term stability of O_2-np NiCu relative to H_2-np NiCu is linked to the kinetically trapped Ni^{2+} state formed during the O_2 treatment, which prevents Ni cluster formation. Catalysts based on metallic Ni, whether monometallic[11, 65-69] or alloyed,[9, 70-73] are prone to accumulate carbon and deactivate by coking.[9, 68, 70-72, 74] By contrast, Cu with its lower reactivity does not break C–C bonds[5, 75-81] consistent with the observation that O_2- and H_2-np Cu exhibit 100% selectivity to acetaldehyde (although at a lower activity than the O_2-np NiCu analog) and do not deactivate. Recent studies have shown that the presence of Ni clusters *vs*. single atoms of Ni on the catalyst leads to a decrease in selectivity for ethanol dehydrogenation.[19, 20] The higher reactivity of Ni clusters allows for C–C bond cleavage and carbon deposition as suggested by CO and CH_4 formation.[19, 68, 70-72] Thus the deactivation of H_2-np NiCu and the increase in the carbon surface concentration on this surface during ethanol exposure in the AP-XPS experiments can be explained by the Ni-rich (20±10 at.% Ni) metallic particles found on the surface of this catalyst. By contrast, carbon deposition on Ni oxide is not significant until 80% of the oxide is reduced coinciding with a decrease in conversion.[82] This suggests that a majority of Ni oxide species need to be reduced in order to initiate deactivation through carbon deposition. The presence of Zn in these CuZn alloy derived catalysts may make the np NiCu catalysts more susceptible to deactivation by carbon deposition as it has been shown that the combined presence of Ni and Zn can lead to deactivation in ethanol steam reforming stemming from the formation of a $Ni_3ZnC_{0.7}$ carbide.[83, 84]

Over time, even the O_2-pretreated np NiCu catalyst slowly deactivates as ethanol or the produced H_2 reduces the kinetically trapped Ni^{2+} leading to more metallic Ni at the surface. Subsequent H_2 treatment of the active O_2-np NiCu accelerates this deactivation mechanism as it completely reduces the Ni^{2+} species to their metallic state thus further increasing the Ni surface concentration.

To maintain the higher activity of NiCu alloys compared to pure Cu beyond 60 h (the longest test runs in this work) will require regeneration of the Ni^{2+} species responsible for the enhanced stability, for example through intermittent O_2 treatments. The regeneration to control the oxidation state of the catalyst surface may also have the beneficial result of carbon removal.[8, 13, 14] Alternatively, one could use a lower Ni concentration NiCu alloy to reduce the tendency for Ni segregation and cluster formation. However, while this approach may result in more stable NiCu catalytic sites, it also is expected to reduce the number of single-atom active sites.

Conclusions

Our work demonstrates that the stability of NiCu alloy catalysts strongly depends on the pretreatment of the catalyst. Specifically, a H_2 pretreatment leads to more reactive, metallic Ni-rich particles, which make this catalyst prone to deactivation, probably because of coking. By contrast, an O_2 pretreatment results in a metastable Ni^{2+} state, correlated with improved activity and long-term stability. The O_2 pretreatment of np NiCu triggers structural changes in the surface region, creating a surface overlayer of copper oxide that covers the Ni originally present at the surface. Simultaneously, the Ni oxidation state transitions to 2+. With subsequent reduction under ethanol dehydrogenation conditions, the surface undergoes another structural and compositional change: The Cu oxide surface layer reduces, and some Ni reappears near the surface in the form of a dilute NiCu alloy, in addition to oxidized Ni-rich particles. In this state, the catalyst exhibits a higher activity than its undoped (Ni-free) counterpart because the NiCu alloy sites reduce the activation energy towards ethanol dehydrogenation. The O_2-pretreated catalyst also shows improved long-term stability as most of the Ni is trapped in its oxidized state where it does not contribute to catalyst deactivation. Similar surface changes driven by exposure to reactive gases at elevated temperatures, either as pretreatment or under reaction conditions, are key to the activity and long-term stability of other alloy catalysts, e.g., selective oxidation reactions on nanoporous AgAu alloys.[85] This study emphasizes the importance of the dynamic changes of catalytic surfaces triggered by exposure to reactive gases as a tool to tune material properties and improve their performance, with implications extending to electrocatalysis, photocatalysis, materials science, metal-based biological applications, and beyond.

Conflicts of interest

There are no conflicts to declare.

Acknowledgements

The authors would like to thank I. Waluyo and D. Stacchiola for their assistance in conducting AP-XPS and NEXAFS experiments and H. Xin for their assistance in STEM characterization (FEI Talos F200X) at Brookhaven National Laboratory. The authors would also like to thank J. Gardner for her assistance with STEM/EDS characterization (JEOL ARM 200F). The authors would also like to thank E. Kaxiras for discussions regarding DFT studies and R. Madix for guiding experiments and valuable discussions. This material is based upon work supported as part of the Integrated Mesoscale Architectures for Sustainable Catalysis (IMASC), an Energy Frontier Research Center funded by the U.S. Department of Energy, Office of Science, Office of Basic Energy Sciences under Award Number DE- SC0012573. Work at LLNL was performed under the auspices of the U.S. Department of Energy by LLNL under Contract DE-AC52-07NA27344. SEM, XPS, and STEM (JEOL ARM 200F) were performed at the Harvard University Center for Nanoscale Systems (CNS), a member of the National Nanotechnology Infrastructure Network (NNIN), which is supported by the National Science Foundation under NSF Award No. 1541959. This research used Beamline 23-ID-2 of the National Synchrotron Light Source II, E-TEM, and STEM (FEI Talos F200X) of the Center for Functional Nanomaterials (CFN), U.S. Department of Energy (DOE) Office of Science User Facilities operated for the DOE Office of Science by Brookhaven National Laboratory under Contract No. DE-SC0012704. **Author contributions:** N.J., M.A.vS., M.M.M., M.B.S., E.A.S., M.F.-S., J.B. and C.M.F. conceived and designed experiments. J.B. and Z.Q. synthesized catalyst materials. N.J., M.A.vS., C.H.W, J.S. D.N.Z, F.X., J.A.B performed materials characterization and catalysis experiments. M.M.M. performed simulations.

Notes and references

1 M. Eckert, G. Fleischmann, R. Jira, H. M. Bolt, and K. Golka, in 'Acetaldehyde', 2006.

2 H. J. Hagemeyer and U. b. S. , in 'Acetaldehyde', 2014.

3 in 'Chemical Data Reporting', 2016.

4 P. Chladek, E. Croiset, W. Epling, and R. R. Hudgins, *Canadian Journal of Chemical Engineering*, 2007, **85**, 917.

5 G. Carotenuto, A. Kumar, J. Miller, A. Mukasyan, E. Santacesaria, and E. E. Wolf, *Catalysis Today*, 2013, **203**, 163.

6 Y.-J. Tu and Y.-W. Chen, *Industrial & Engineering Chemistry Research*, 2001, **40**, 5889.

7 S. Hanukovich, A. Dang, and P. Christopher, *ACS Catalysis*, 2019, **9**, 3537.

8 J. M. Conesa, M. V. Morales, C. López-Olmos, I. Rodríguez-Ramos, and A. Guerrero-Ruiz, *Applied Catalysis A: General*, 2019, **576**, 54.

9 J. De Waele, V. V. Galvita, H. Poelman, M. Gabrovska, D. Nikolova, S. Damyanova, and J. W. Thybaut, *Applied Catalysis A: General*, 2020, **591**, 117401.

10 P. H. Finger, T. A. Osmari, M. S. Costa, J. M. C. Bueno, and J. M. R. Gallo, *Applied Catalysis A: General*, 2020, **589**, 117236.

11 S. Luo, H. Song, D. Philo, M. Oshikiri, T. Kako, and J. Ye, *Applied Catalysis B: Environmental*, 2020, **272**, 118965.

12 G. Garbarino, P. Riani, M. Villa García, E. Finocchio, V. Sanchez Escribano, and G. Busca, *Catalysis Today*, 2020, **354**, 167.

13 D. Yu, W. Dai, G. Wu, N. Guan, and L. Li, *Chinese Journal of Catalysis*, 2019, **40**, 1375.

14 H. Zhang, H.-R. Tan, S. Jaenicke, and G.-K. Chuah, *Journal of Catalysis*, 2020, **389**, 19.

15 P. Daorattanachai, S. Totong, and N. Laosiripojana, *Journal of Sustainable Energy & Environment*, 2018, **9**, 41.

16 M. Ohira, H. Liu, D. He, Y. Hirata, M. Sano, T. Suzuki, and T. Miyake, *Journal of the Japan Petroleum Institute*, 2018, **61**, 205.

17 M. Rosset and O. W. Perez-Lopez, *Reaction Kinetics, Mechanisms and Catalysis*, 2019, **126**, 497.

18 I. C. Freitas, J. M. R. Gallo, J. M. C. Bueno, and C. M. P. Marques, *Topics in Catalysis*, 2016, **59**, 357.

19 J. Shan, N. Janvelyan, H. Li, J. Liu, T. M. Egle, J. Ye, M. M. Biener, J. Biener, C. M. Friend, and M. Flytzani-Stephanopoulos, *Applied Catalysis B: Environmental*, 2017, **205**, 541.

20 J. Shan, J. Liu, M. Li, S. Lustig, S. Lee, and M. Flytzani-Stephanopoulos, *Applied Catalysis B: Environmental*, 2018, **226**, 534.

21 G. Giannakakis, A. Trimpalis, J. Shan, Z. Qi, S. Cao, J. Liu, J. Ye, J. Biener, and M. Flytzani-Stephanopoulos, *Topics in Catalysis*, 2018, **61**, 475.

22 DOE, *U.S. Department of Energy (DOE), Office of Basic Energy Sciences (BES)*, 2017.

23 F. Tao, M. E. Grass, Y. Zhang, D. R. Butcher, J. R. Renzas, Z. Liu, J. Y. Chung, B. S. Mun, M. Salmeron, and G. A. Somorjai, *Science*, 2008, **322**, 932.

24 J. E. S. van der Hoeven, T. A. J. Welling, T. A. G. Silva, J. E. van den Reijen, C. La Fontaine, X. Carrier, C. Louis, A. van Blaaderen, and P. E. de Jongh, *ACS Nano*, 2018, **12**, 8467.

25 C. H. Wu, C. Liu, D. Su, H. L. Xin, H.-T. Fang, B. Eren, S. Zhang, C. B. Murray, and M. B. Salmeron, *Nature Catalysis*, 2019, **2**, 78.

26 S. Zafeiratos, S. Piccinin, and D. Teschner, *Catalysis Science & Technology*, 2012, **2**, 1787.

27 F. Tao, S. Zhang, L. Nguyen, and X. Zhang, *Chemical Society Reviews*, 2012, **41**, 7980.

28 Z. Wang, L. Fang, I. Cotton, and R. Freer, *Materials Science and Engineering: B*, 2015, **198**, 86.

29 H. Shinotsuka, S. Tanuma, C. J. Powell, and D. R. Penn, *Surface and Interface Analysis*, 2015, **47**, 871.

30 G. Kresse and J. Furthmüller, *Computational Materials Science*, 1996, **6**, 15.

31 G. Kresse and J. Hafner, *Physical Review B*, 1993, **47**, 558.

32 J. P. Perdew, K. Burke, and M. Ernzerhof, *Physical Review Letters*, 1996, **77**, 3865.

33 G. Kresse and D. Joubert, *Physical Review B*, 1999, **59**, 1758.

34 P. E. Blöchl, *Physical Review B*, 1994, **50**, 17953.

35 A. Tkatchenko and M. Scheffler, *Physical Review Letters*, 2009, **102**, 073005.

36 G. Hautier, S. P. Ong, A. Jain, C. J. Moore, and G. Ceder, *Physical Review B*, 2012, **85**, 155208.

37 X. Rocquefelte, M. H. Whangbo, A. Villesuzanne, S. Jobic, F. Tran, K. Schwarz, and P. Blaha, *Journal of Physics: Condensed Matter*, 2010, **22**, 045502.

38 T. Egle, C. Barroo, N. Janvelyan, A. C. Baumgaertel, A. J. Akey, M. M. Biener, C. M. Friend, D. C. Bell, and J. Biener, *ACS Applied Materials & Interfaces*, 2017, **9**, 25615.

39 W. H. Cassinelli, L. Martins, M. Magnani, S. H. Pulcinelli, V. Briois, and C. V. Santilli, *RSC Advances*, 2016, **6**, 20453.

40 W. H. Cassinelli, L. Martins, A. R. Passos, S. H. Pulcinelli, A. Rochet, V. Briois, and C. V. Santilli, *ChemCatChem*, 2015, **7**, 1668.

41 C.-Y. Chen, in 'Catalyst Regeneration via Reduction with Hydrogen', US.

42 S. Modak and B. C. Khanra, *Physical Review B*, 1986, **34**, 5909.

43 J. H. Sinfelt, J. L. Carter, and D. J. C. Yates, *Journal of Catalysis*, 1972, **24**, 283.

44 S. K. Beaumont, S. Alayoglu, V. V. Pushkarev, Z. Liu, N. Kruse, and G. A. Somorjai, *Faraday Discussions*, 2013, **162**, 31.

45 L. Pielsticker, I. Zegkinoglou, N. J. Divins, H. Mistry, Y.-T. Chen, A. Kostka, J. A. Boscoboinik, and B. R. Cuenya, *The Journal of Physical Chemistry B*, 2018, **122**, 919.

46 J. A. Rodriguez, J. Y. Kim, J. C. Hanson, M. Pérez, and A. I. Frenkel, *Catalysis Letters*, 2003, **85**, 247.

47 C.-S. Chen, J.-H. You, J.-H. Lin, C.-R. Chen, and K.-M. Lin, *Catalysis Communications*, 2008, **9**, 1230.

48 S. D. Robertson, B. D. McNicol, J. H. De Baas, S. C. Kloet, and J. W. Jenkins, *Journal of Catalysis*, 1975, **37**, 424.

49 K. V. Manukyan, A. G. Avetisyan, C. E. Shuck, H. A. Chatilyan, S. Rouvimov, S. L. Kharatyan, and A. S. Mukasyan, *The Journal of Physical Chemistry C*, 2015, **119**, 16131.

50 Q. Jeangros, T. W. Hansen, J. B. Wagner, C. D. Damsgaard, R. E. Dunin-Borkowski, C. Hébert, J. Van herle, and A. Hessler-Wyser, *Journal of Materials Science*, 2013, **48**, 2893.

51 R. D. Leapman, L. A. Grunes, and P. L. Fejes, *Physical Review B*, 1982, **26**, 614.

52 C. R. Helms and K. Y. Yu, *Journal of Vacuum Science and Technology*, 1975, **12**, 276.
53 T. T. Tsong, Y. S. Ng, and S. B. J. McLane, *Journal of Applied Physics*, 1980, **51**, 6189.
54 I. Kamiya, T. Hashizume, A. Sakai, T. Sakurai, and H. Pickering, *Journal de Physique Colloques*, 1986, **47**, 195.
55 Y. Takasu, H. Shimizu, S.-i. Maru, and Y. Matsuda, *Surface Science*, 1976, **61**, 279.
56 J. E. Castle, *Corrosion Science*, 1979, **19**, 475.
57 J. E. Castle and M. Nasserian-Riabi, *Corrosion Science*, 1975, **15**, 537.
58 R. L. Souchet, M.; Miche, P.; Weber, S.; Scherrer, S., *Analusis*, 1993, **21**, 173.
59 E. F. L. Marano, Danilo; Castellero, Alberto; Baricco, Marcello, *Met. Mater. Int.*, 2016, **22**, 305.
60 G. Zhou and J. C. Yang, *Surface Science*, 2003, **531**, 359.
61 M. Lortie, R. Isaifan, Y. Liu, and S. Mommers, *International Journal of Chemical Engineering*, 2015, **2015**, 9.
62 J. Bian, M. Xiao, S. Wang, X. Wang, Y. Lu, and Y. Meng, *Chemical Engineering Journal*, 2009, **147**, 287.
63 F. Studt, F. Abild-Pedersen, Q. Wu, A. D. Jensen, B. Temel, J.-D. Grunwaldt, and J. K. Nørskov, *Journal of Catalysis*, 2012, **293**, 51.
64 K. P. Kepp, *Inorganic Chemistry*, 2016, **55**, 9461.
65 S. E. Olesen, K. J. Andersson, C. D. Damsgaard, and I. Chorkendorff, *The Journal of Physical Chemistry C*, 2017, **121**, 15556.
66 J. Barrientos, N. Gonzalez, M. Boutonnet, and S. Järås, *Topics in Catalysis*, 2017, **60**, 1276.
67 H. H. Gierlich, M. Fremery, A. Skov, and J. R. Rostrup-Nielsen, in 'Deactivation Phenomena of a Ni-based Catalyst for High Temperature Methanation', ed. B. Delmon and G. F. Froment, 1980.
68 V. Fierro, O. Akdim, and C. Mirodatos, *Green Chemistry*, 2003, **5**, 20.
69 C. Montero, A. Ochoa, P. Castaño, J. Bilbao, and A. G. Gayubo, *Journal of Catalysis*, 2015, **331**, 181.
70 C. Anjaneyulu, L. O. O. d. Costa, M. C. Ribeiro, R. C. Rabelo-Neto, L. V. Mattos, A. Venugopal, and F. B. Noronha, *Applied Catalysis A: General*, 2016, **519**, 85.
71 A. J. Vizcaíno, A. Carrero, and J. A. Calles, *International Journal of Hydrogen Energy*, 2007, **32**, 1450.
72 G. Zeng, Q. Liu, R. Gu, L. Zhang, and Y. Li, *Catalysis Today*, 2011, **178**, 206.
73 Y.-G. Chen, K. Tomishige, K. Yokoyama, and K. Fujimoto, *Journal of Catalysis*, 1999, **184**, 479.
74 J. Lahiri, T. Miller, L. Adamska, I. I. Oleynik, and M. Batzill, *Nano Letters*, 2011, **11**, 518.
75 K. Inui, T. Kurabayashi, and S. Sato, *Applied Catalysis A: General*, 2002, **237**, 53.
76 D. Gao, Y. Feng, H. Yin, A. Wang, and T. Jiang, *Chemical Engineering Journal*, 2013, **233**, 349.
77 K.-D. Jung, O.-S. Joo, S.-H. Han, S.-J. Uhm, and I.-J. Chung, *Catalysis Letters*, 1995, **35**, 303.
78 A. Musˇicˇ, J. Batista, and J. Levec, *Applied Catalysis A: General*, 1997, **165**, 115.
79 K. Inui, T. Kurabayashi, and S. Sato, *Journal of Catalysis*, 2002, **212**, 207.
80 V. Z. Fridman and A. A. Davydov, *Journal of Catalysis*, 2000, **195**, 20.
81 M. M. L. Tormena and R. M. Pontes, *Molecular Catalysis*, 2020, **482**, 110694.
82 P. Cho, T. Mattisson, and A. Lyngfelt, *Industrial & Engineering Chemistry Research*, 2005, **44**, 668.
83 M. N. Barroso, M. F. Gomez, L. A. Arrúa, and M. C. Abello, *Applied Catalysis A: General*, 2006, **304**, 116.
84 A. E. Galetti, M. F. Gomez, L. A. Arrúa, and M. C. Abello, *Applied Catalysis A: General*, 2008, **348**, 94.
85 B. Zugic, M. A. van Spronsen, C. Heine, M. M. Montemore, Y. Li, D. N. Zakharov, S. Karakalos, B. A. J. Lechner, E. Crumlin, M. M. Biener, A. I. Frenkel, J. Biener, E. A. Stach, M. B. Salmeron, E. Kaxiras, R. J. Madix, and C. M. Friend, *Journal of Catalysis*, 2019, **380**, 366.

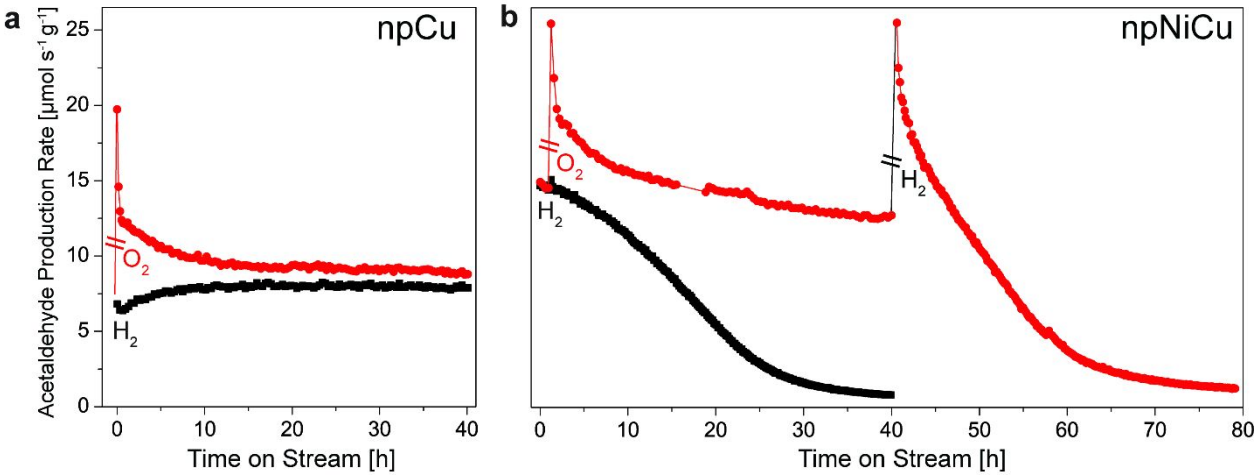

Figure 1. Ethanol-to-acetaldehyde conversion activity of np Cu and np NiCu after various pretreatments: (a) np Cu displays stable activity towards acetaldehyde production after 10 h regardless of H_2 (black) or O_2 (red) pretreatments; (b) O_2 pretreated np NiCu shows improved reactivity and stability compared to H_2 pretreated np NiCu. The latter leads to rapid catalyst deactivation. Reaction conditions: 250 °C, 50 mL min^{-1}, 6 vol.% ethanol/He. H_2 pretreatment: 350 °C, 20 mL min^{-1}, 10 vol.% H_2/He. O_2 pretreatment: 250 °C, 50 mL min^{-1}, 20 vol.% O_2/He. All exposures were at atmospheric pressure (760 Torr).

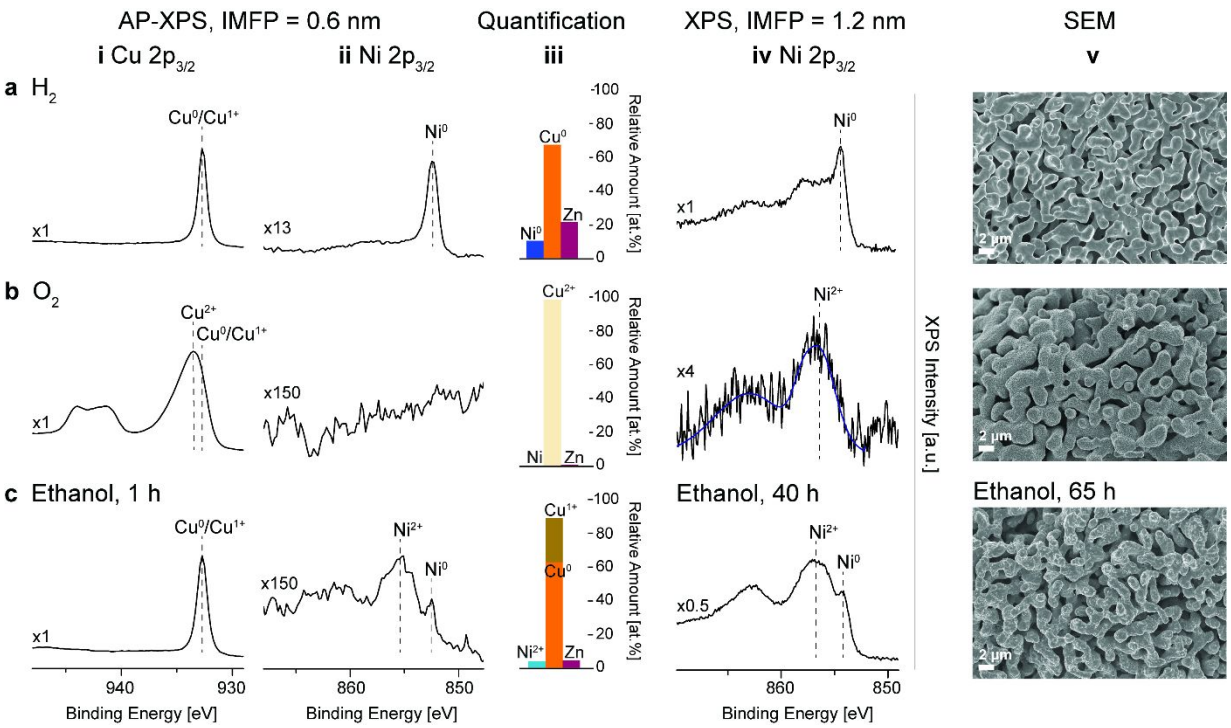

Figure 2. AP-XPS (i-iii), *ex situ* XPS (iv), and SEM (v) data reveal the compositional, chemical-state, and morphological changes of np NiCu during H_2 and O_2 pretreatments and during ethanol-to-acetaldehyde conversion: a) after *in situ* H_2 pretreatment (350 °C, 1 Torr, 1 h), Cu and Ni are in their metallic states (i-iv) while the surface morphology is smooth (v); b) after oxidation (250 °C, 1 Torr, 1 h), Cu is oxidized and Ni is no longer detected by AP-XPS (i-iii), a small amount of oxidized Ni is detected by *ex situ* XPS due to its higher IMFP (iv), and the surface is roughened (v); c) after subsequent ethanol exposure (250 °C, 0.2 Torr, 1 h), (i) surface Cu becomes reduced again and a small amount of oxidized Ni emerges (i-iv) while the surface smoothens after extended ethanol exposure (v). AP-XPS data were collected under ultra-high vacuum conditions at room temperature for a) and b), while c) is collected in 0.2 Torr ethanol at 250 °C. Kinetic energies of exiting electrons in the AP-XPS are 200 eV for both Cu and Ni, yielding an inelastic mean free path of 0.6 nm or 1–3 atomic layers. The *ex situ* inelastic mean free path is 1.2 nm or 4–6 atomic layers. To emphasize the surface morphology changes induced by interaction with reactive gases (v) shows representative SEM images of np NiCu with larger ligaments.

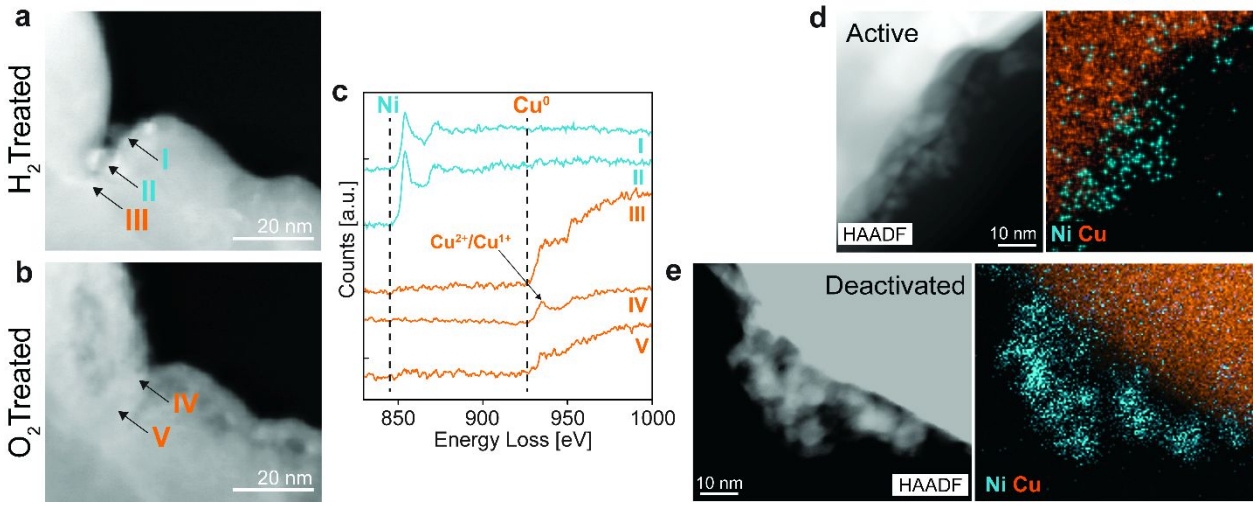

Figure 3. E-TEM (a, b) and EELS (c) analysis of np NiCu illustrates the overgrowth of Cu oxide covering Ni nanoparticles at the surface of a np NiCu ligament. *Ex situ* STEM and EDS mapping (d, e) show Ni-rich nanoparticles resurfacing with subsequent ethanol exposure and on the deactivated catalyst surface. *In situ* aberration corrected high-angle annular dark-field (ac-HAADF)-STEM and EELS data were obtained: a) after reduction in H_2 (350 °C, 1 Torr, 1 h) and exposure to ethanol (250 °C, 0.2 Torr, 17 h) showing particles at the sample surface. EELS analysis indicates the particles outside the Cu ligament are Ni (i-iii). b) After oxidation (250 °C, 1 Torr, 1 h), a rough copper oxide layer covers the surface (iv), which is more metallic towards the bulk (v), and no Ni was detectable. All data were collected in vacuum at room temperature. d) After O_2 treatment and exposure to ethanol (40 h), the reappearance of oxidized Ni nanoparticles and reduction of the copper oxide overlayer are observed as revealed by the *ex situ* HAADF image and the corresponding elemental map. e) After H_2 treatment, O_2-treated np NiCu completely deactivates (Figure 1b, 40–80 h) and exhibits dense Ni nanoparticles due to its metallic nature as shown by the bright areas in the *ex situ* HAADF image and the corresponding elemental map. The large bright features in the HAADF images (d, e) are the np NiCu catalyst bulk (which is strongly scattering).

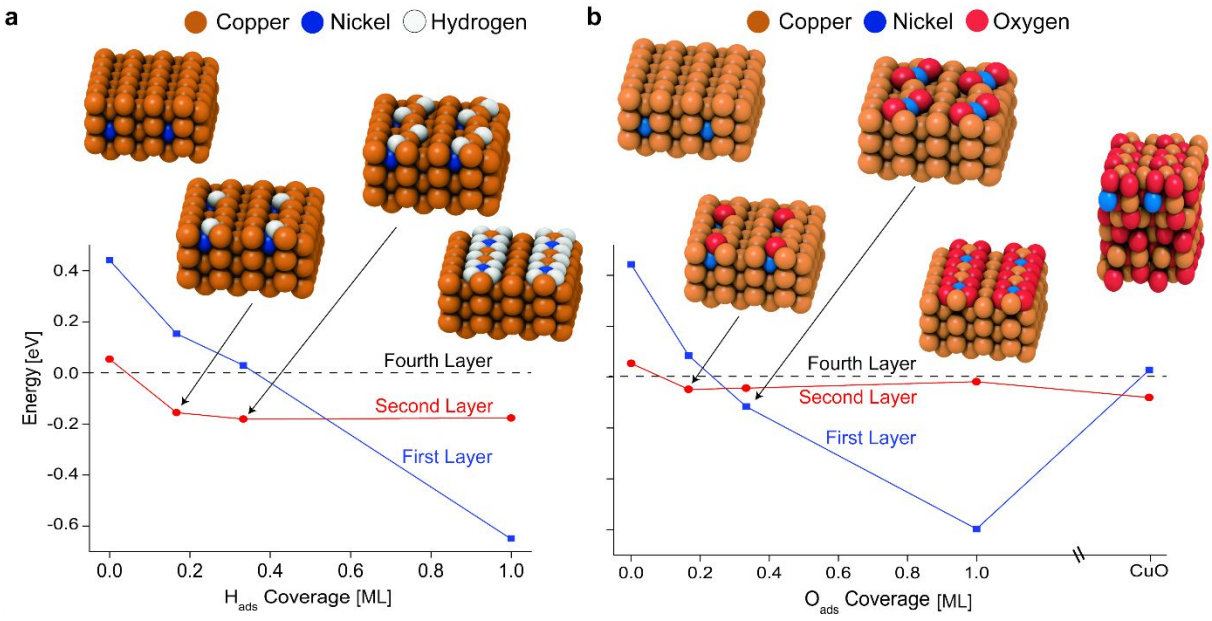

Figure 4. DFT modeling of NiCu alloys reveals that surface segregation of Ni depends on hydrogen and oxygen coverage of the surface. a) Increasing H coverage from 0 to 1 ML brings Ni from the bulk to the topmost layer. b) Increasing O coverage from 0 to 1 ML brings Ni from the bulk (fourth layer) to the first layer. With complete oxidation of Cu to CuO, Ni prefers to be in the second layer, reversing the trend. Surface energies of Ni in the first three atomic layers of Cu(110) and CuO(111) were calculated relative to Ni in the fourth layer with various surface coverages of the adsorbates. Surface energies of Ni in the third layer were roughly the same as the fourth layer and thus are not included. The lowest energy configuration at each coverage is shown above each data point.

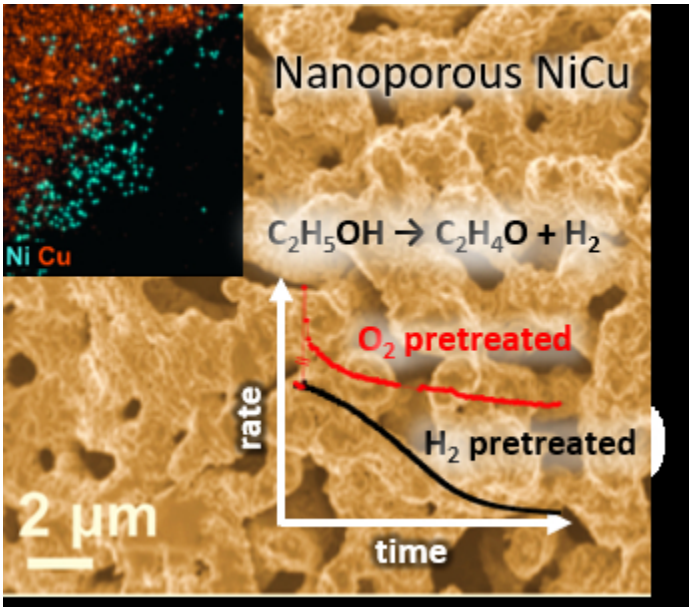
Nanoporous NiCu
Ni Cu
$C_2H_5OH \rightarrow C_2H_4O + H_2$
O_2 pretreated
H_2 pretreated
rate
time
2 µm